Nanoscale

PAPER

View Article Online
View Journal



Cite this: DOI: 10.1039/d5nr04204f

# Nanoscale control over single vortex motion in an unconventional superconductor

Sang Yong Song,[a] Chengyun Hua,[b] Gábor B. Halász,[b] Wonhee Ko,[c] Jiaqiang Yan,[b] Benjamin J. Lawrie[b] and Petro Maksymovych *[a,d]

Precise control of superconducting vortices is crucial for studying vortex dynamics and vortex braiding. We propose a new method to pull vortex lines in the layered superconductor FeSe using a scanning tunneling microscope (STM) tip. Weak contact of the STM tip with the FeSe surface locally reduces the superconducting gap, thereby creating a tunable vortex pinning potential on the nanometer scale. This enables controlled vortex line deformation even in dense vortex lattices. Analytical modeling reveals that the deformation strength scales logarithmically with conductance and depends on tip geometry. Our findings point to local strain-induced gap suppression as the mechanism for STM-mediated vortex manipulation, providing a fundamental insight relevant to vortex behavior in the context of quantum information studies.

Received 8th October 2025,
Accepted 22nd February 2026

DOI: 10.1039/d5nr04204f

rsc.li/nanoscale



## Introduction

For a type-II superconductor exposed to a magnetic field greater than the lower critical field, quantized magnetic fluxes penetrate the superconductor.[1] Each magnetic flux quantum breaks Cooper pairs and induces a circulating supercurrent that creates a vortex line, a cylindrical region of normal metal with a radius equivalent to the superconducting coherence length.[2,3] Due to the Lorentz force, vortex lines repel each other and arrange into a lattice structure. These vortex lines behave like interacting elastic strings and can be partially pinned and deformed by defects.[4–7]

A growing interest in understanding and controlling superconducting vortices in recent years emerges from the potential for manipulating Majorana modes that are predicted to occur in the vortex core in topological superconductors.[8–11] Control over such Majorana zero modes is crucial for the fundamental understanding of non-Abelian statistics and in the basic study of topologically protected qubits.[12–18]

Individual vortex manipulation is challenging in both bulk superconductors and thin films, because vortex lines are partially pinned by defects and also exhibit strong vortex-vortex repulsion. Previously, several approaches to manipulate vortices through optical[19] and resistive[20] heating, mechanical stress,[21] and magnetic force[6,22–25] have been demonstrated. Furthermore, vortices have recently been manipulated by electronic devices,[26,27] and it has been theoretically proposed to use domain walls to manipulate vortices.[28] However, all these techniques have limited spatial resolution, and as a result, they cannot be used for the individual manipulation of vortices separated by less than a few hundred nanometers.

Scanning tunneling microscopy (STM) is a natural candidate to consider for this purpose owing to its sensitivity to the vortex states, atomic spatial resolution, and a growing number of reports on the observation of Majorana zero modes through tunneling spectroscopy.[10,11,29–31] STM can also famously manipulate adsorbed atoms and molecules with atomic-scale precision.[32–34] Yet, in most cases – such as nonmagnetic tips and small tunneling conductance – the tip of the tunneling microscope would not exert sufficient force onto the vortex line. Therefore, previous attempts to manipulate vortices with an STM tip required local melting of the superconducting state.[20] In addition, Kremen *et al.* manipulated vortices with the formation of a large and strong mechanical contact (~100 nm) on niobium (Nb) and niobium nitride (NbN) thin film using a fabricated tip of a superconducting quantum interference device (SQUID) chip.[21] Although vortex manipulation has been achieved in these cases, the precise origin of the forces, as well as the applicability of these methods to dense vortex lattices remain uncertain.

Here, we reveal an effective approach to manipulate single vortices in Fe-based superconductors. We found that wrinkles formed by strain in the surface layer can effectively pin vor-

[a]Center for Nanophase Materials Sciences, Oak Ridge National Laboratory, Oak Ridge, TN 3781, USA. E-mail: pmaksym@clemson.edu
[b]Materials Science and Technology Division, Oak Ridge National Laboratory, Oak Ridge, TN 37831, USA
[c]Department of Physics and Astronomy, University of Tennessee at Knoxville, Knoxville, TN 37996, USA
[d]Department of Materials Science and Engineering, Clemson University, Clemson, SC 29634, USA

tices, thereby altering the configuration of the vortex lattice. Based on this observation, we determined whether vortex line deformation could be induced by creating a trapping potential with an STM tip in weak physical contact with a superconducting surface. On FeSe, this approach revealed an unexpectedly large vortex line deformation. Furthermore, we confirmed that under such physical contact conditions for FeSe, which has two superconducting gaps, the spectral weight of the large gap is suppressed but the small gap remains. The same gap suppression occurs in wrinkles where strain is present. The local attractive potential on the vortex line is easily induced in this case, compared to previously studied BCS superconductors,[35] and ultimately enables deformation of the vortex lines even in dense vortex lattices. One possible mechanism for the local suppression of the superconducting gap is strain induced beneath the STM tip, which reduces superconducting gaps in FeSe due to several possible pair-breaking interactions. We further applied an analytical model for vortex pinning by an external potential and revealed that the deformation of the vortex line logarithmically increases as a function of contact conductance. Moreover, the contact geometry strongly affects the strength of the trapping potential. We anticipate that this approach will work on many Fe-based superconductors, particularly those with multigap structures, enabling fundamental studies of both single vortex dynamics and the susceptibility of vortex bound states to local strain, along with the eventual control of vortex–vortex interactions.

## Results and discussion

### Effects of wrinkles and twin boundaries on vortices

First, we discuss peculiar properties of vortex lines near wrinkles in FeSe. Fig. 1a shows a differential conductance map at −2.5 mV illustrating the vortex lattice configuration (yellow dots) at 0.13 T in the presence of twin boundaries (green arrows) and a wrinkle (orange dotted line) (the corresponding topographic data is provided in Fig. 1b and d.) A Voronoi diagram (black lines in Fig. 1a) was added to facilitate visualization of the vortex lattice. Twin boundaries strongly pin vortices, altering the lattice configuration and reducing the intervortex distance. The wrinkle also pins vortices; although it barely reduces the intervortex distance, it can substantially alter the vortex configuration. It is known that FeSe has a main

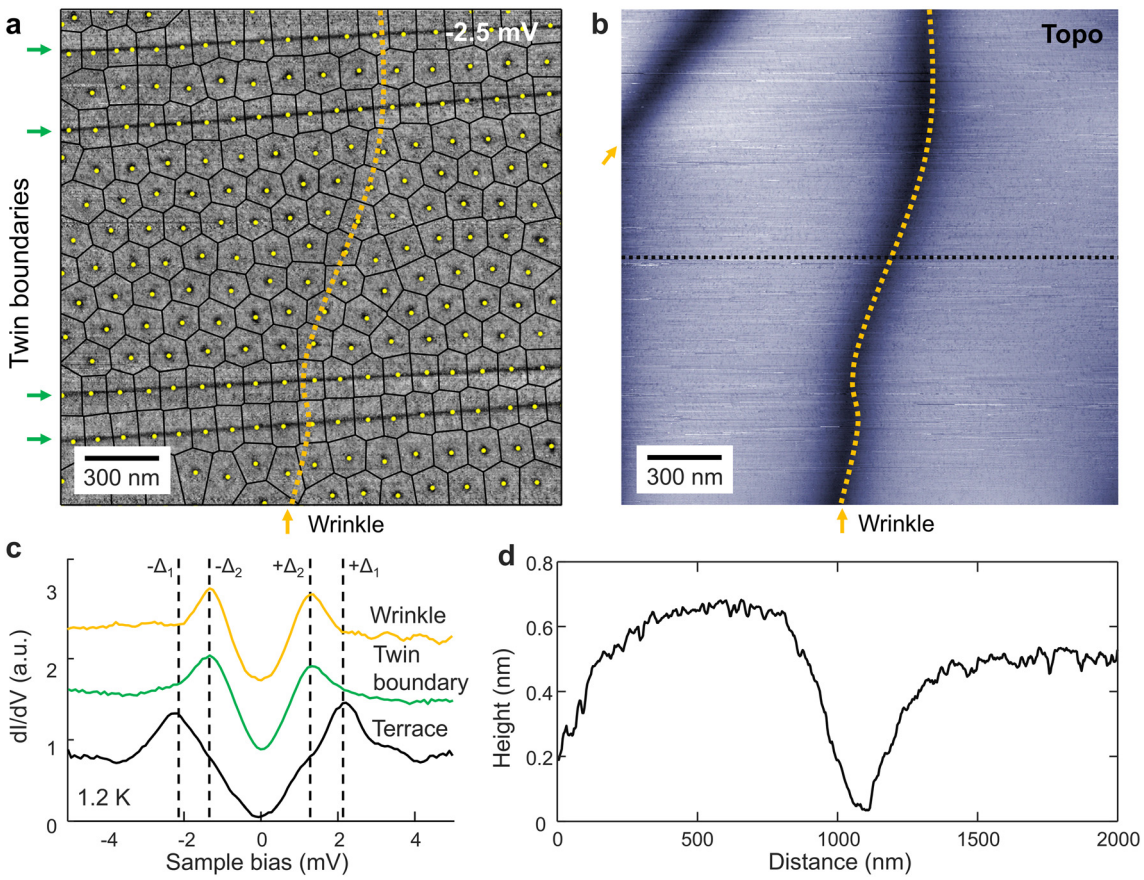


**Fig. 1** Modification of the vortex lattice near the twin boundaries and wrinkle. (a) Differential conductance map at −2.5 mV on FeSe under 0.14 T ($V_{bias}$ = −2.5 mV, $I$ = 100 pA). Yellow dots indicate vortex lattice, and black lines represent the Voronoi diagram. Twin boundaries are located at the positions marked by the green arrows, and a wrinkle is aligned with the orange dotted line. (b) The topographic image corresponding to the same region as in the conductance map in (a) ($V_{bias}$ = −2.5 mV, $I$ = 100 pA). (c) d$I$/d$V$ spectra acquired on the terrace (black), at the center of the twin boundary (green), and at the center of the wrinkle (orange) of FeSe. (d) Topographic line profile along the black dashed line in panel (b).

gap $\Delta_1$ (2–3 mV) and a small gap $\Delta_2$ appearing as a shoulder (~1 mV) (black d$I$/d$V$ curve in Fig. 1c).[36,37] At both twin boundaries and wrinkles, we observe a common suppression of the spectral weight of gap $\Delta_1$, while $\Delta_2$ remains (Fig. 1c and Fig. S1, SI). In terms of vortex line energy, such a local gap reduction naturally acts as a strong pinning potential to alter the vortex configuration. A natural question arises whether the STM tip itself can create a sufficiently large and strong trapping potential.

### Local modification of superconducting gap

To this end, we first investigated the impact of tip-induced strain on the superconducting gap (Fig. 2). We gradually extend the STM tip toward the surface, up to 1.2 nm from the set point $V_{bias}$ = 8 mV, and $I$ = 1 nA ($0.002G_0$) ($z$ = 0 pm). $G_0$ is the conductance quantum $2e^2/h$. Here, the tip extension is the ideal value from the applied piezo voltage, but it is likely smaller due to tip–sample interactions. As the STM tip approaches the surface, the conductance trace changes rapidly (blue circles in Fig. 2b) and then begins to increase linearly (red circles in Fig. 2b). The first abrupt change in the conductance trace (blue circles in Fig. 2b) is likely due to the instability of the atomic contact condition. Moreover, the linear increase in conductance (as shown by the red circles in the inset in Fig. 2b) can be interpreted as reflecting a linear increase in the tip–sample contact area. The superconducting gaps of FeSe change significantly during tip contact to the surface. Specifically, the spectral weight of the small gap $\Delta_2$ is relatively enhanced (blue arrows in Fig. 2c) in the near atomic contact condition ($0.13G_0$). Furthermore, in the regime of $0.32$–$1.6G_0$, the spectral weight of the large gap $\Delta_1$ is suppressed while the small gap $\Delta_2$ remains (red arrows in Fig. 2c). The remaining small gap $\Delta_2$ is reminiscent of the remaining superconducting gap near a wrinkle defect (orange spectrum in Fig. 1c) or a twin boundary (green spectrum in Fig. 1c) on the FeSe surface (Fig. S1a–d, SI). Interestingly, when the conductance is further increased over $2.29G_0$, the coherence peak of the small gap $\Delta_2$ becomes broader, while the interior of the gap becomes narrower (dark red spectra in Fig. 2c). We note that possible voltage division effects due to external circuitry are quantitatively negligible in our setup. Based on the known output resistance of the bias attenuator and the minimum junction resistance used here, the resulting reduction of the actual tip–sample voltage is below a few percent, leading to peak shifts on the order of several tens of μV, which is far smaller than the energy shifts observed in Fig. 2 (see note S1, SI). We find that once a stable tip apex is established, the conductance traces and d$I$/d$V$ spectra exhibit overall similar trends across repeated measurements (Fig S2, SI). In addition, in the contact and near-contact regimes, the measured d$I$/d$V$ does not directly represent the local density of states in a Tersoff–Hamann sense and may include transport related contributions. Nevertheless, while the high-conductance d$I$/d$V$ curves cannot be directly interpreted as the LDOS, we observe a gradual reduction of the superconducting gap upon approaching contact (Fig. 2c). This gap reduction induced by the STM tip provides the primary origin of the trapping potential in our method.

### Vortex displacement by local forces

The evolution of superconducting vortices with increasing conductance value is shown in Fig. 3. The most notable change is a dramatic enlargement of the vortex features. Fig. 3a–e show differential conductance maps at −2.5 mV of the apparently expanded vortex cores as the conductance value increases from $0.51G_0$ (100 nA) to $3.10G_0$ (600 nA) (set bias: $V_{bias}$ = −2.5 mV). The apparent size of the vortex core is reversible (Fig. S3, SI) and increases from 30 nm up to as much as 140 nm at $3.10G_0$ on the terrace. Furthermore, we measured d$I$/d$V$ spectral maps to investigate the electronic structure of the expanded vortex. Fig. 4c and d show zero-bias differential conductance maps, which are extracted from d$I$/d$V$ spectral maps of the vortex

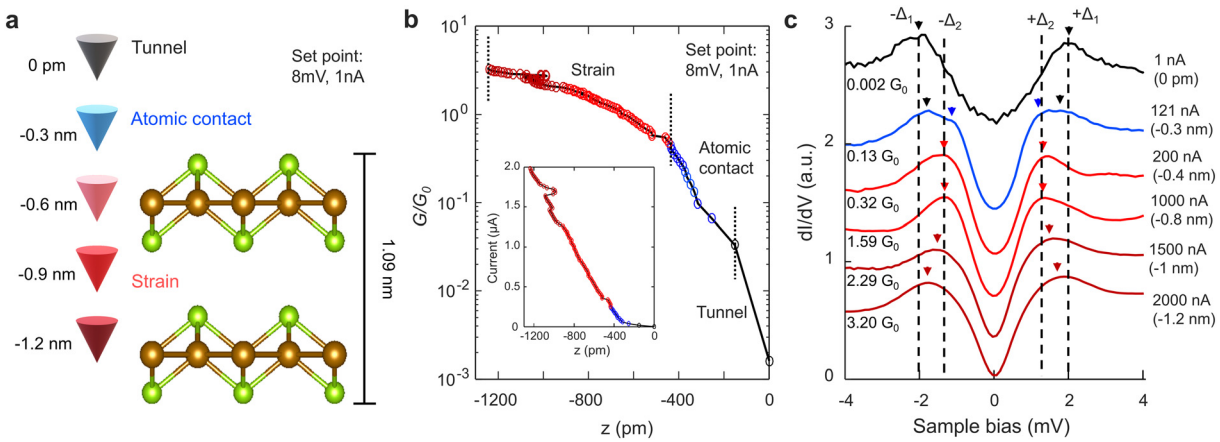


**Fig. 2** STM tip induced reduction of the superconducting gap. (a) Schematic image of the tip positions relative to the FeSe atomic layers. The tip extension distance shown here is the ideal displacement of the piezo tube, obtained from the voltage applied to the piezo. (b) Conductance and current (inset) curves with respect to the tip positions (set point: $I$ = 100 pA, $V_{bias}$ = 8 mV). (c) The variation of superconducting gaps on the FeSe surface from tunneling ($0.002G_0$) to $3.20G_0$. Here, $G_0 = 2e^2/h$ is the conductance quantum.

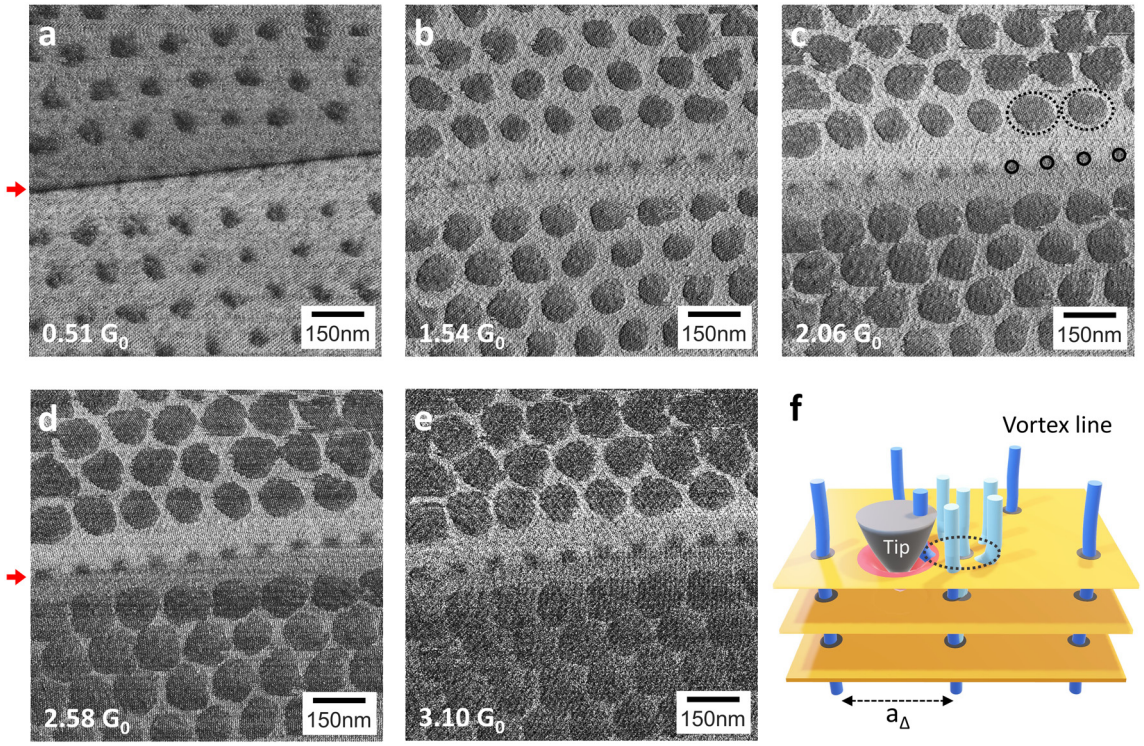


**Fig. 3** Evolution of vortex images with increasing influence of the STM tip. (a–e) Large size maps of expanded vortex cores on the terrace and the twin boundary at $0.51G_0$ (100 nA), $1.54G_0$ (300 nA), $2.06G_0$ (400 nA), $2.58G_0$ (500 nA), and $3.1G_0$ (600 nA) measured by Tip1. Red arrow indicates the position of the twin boundary. (f) Schematic image of deformation of vortex line near the tip induced wrinkle (red curved area).

cores on the terrace and on the twin boundary (black dashed box in Fig. 4a) at each starting point $0.003G_0$ (tunneling), and $1.57G_0$ (setpoint: $V_{bias}$ = 5 mV and 1 nA, and 600 nA, respectively). From the d$I$/d$V$ spectral map, we confirmed that the apparent size of the vortex core is correlated to the magnitude of the starting conductance (set point) rather than the current at each bias (Fig. S4 and S5, SI). For example, at an initial conductance of $1.57G_0$ (setpoint: $V_{bias}$ = 5 mV and $I$ = 600 nA), the size of the vortex is the same at 0.04 mV (0.7 nA) and at 3.6 mV (407 nA), despite two orders of magnitude difference in the current (Fig. S4b and d, SI). This observation substantially rules out current-induced processes, such as current-driven force and thermal effects, as the causes of the increased apparent size of the vortex. In addition, we occasionally observed changes in the vortex array during mapping at high conductance values (Fig. S6, SI).

We propose that the apparent enlargement of the vortex image corresponds to the locations where the vortex line is deformed by the tip-induced wrinkle (the red curved area in Fig. 3f), which induces gap reduction and serves as the origin of the trapping potential. One of the pieces of evidence supporting our interpretation is that the vortex bound states are observed across the expanded vortices, as seen at the blue arrows in Fig. 4h for setpoint $1.57G_0$ (600 nA). Fig. 4g and h show the spatial variation of vortex bound states across green dotted arrows at $0.003G_0$ (in Fig. 4c) and $1.57G_0$ (in Fig. 4d), respectively. Detailed spatial variations of vortex bound states at $0.003G_0$ and $1.57G_0$ are shown in Fig. S7 and S8 (SI). The observation of vortex bound states alone rules out spurious artifacts, such as adsorbates and topographic damage as the possible origin of the expanded vortex images. We also acknowledge that transport-related effects such as Andreev reflection and changes in junction transparency may influence the spectra in the contact regime. However, the spatially resolved evolution of the d$I$/d$V$ line shape allows us to reliably distinguish vortex cores from superconducting regions, independent of a direct LDOS interpretation.

Our conclusions are further supported by the stark contrast between the vortices on the terrace and those pinned by the twin boundaries – naturally occurring planar defects due to the tetragonal to orthorhombic phase transition in FeSe below 90 K.[38,39] Twin boundaries suppress the large superconducting gap $\Delta_1$ (Fig. 1c and Fig. S1d, SI) and create a strong vortex pinning potential.[40–42] In contrast to the vortices on the terrace, vortices along the twin boundary barely expand at high conductance values in Fig. 3 and 4d. In addition, Fig. 4f shows the spatial variation of d$I$/d$V$ spectra across the vortex core on the twin boundary (orange dotted arrow in Fig. 4d) at $1.57G_0$. On the twin boundary, the spatial distribution of vortex-bound states remains virtually unchanged in spectroscopy (black arrow in Fig. 4f). The twin boundaries also reinforce the hypothesis that the tip-induced changes to the superconducting gap structure are responsible for vortex line deformations.

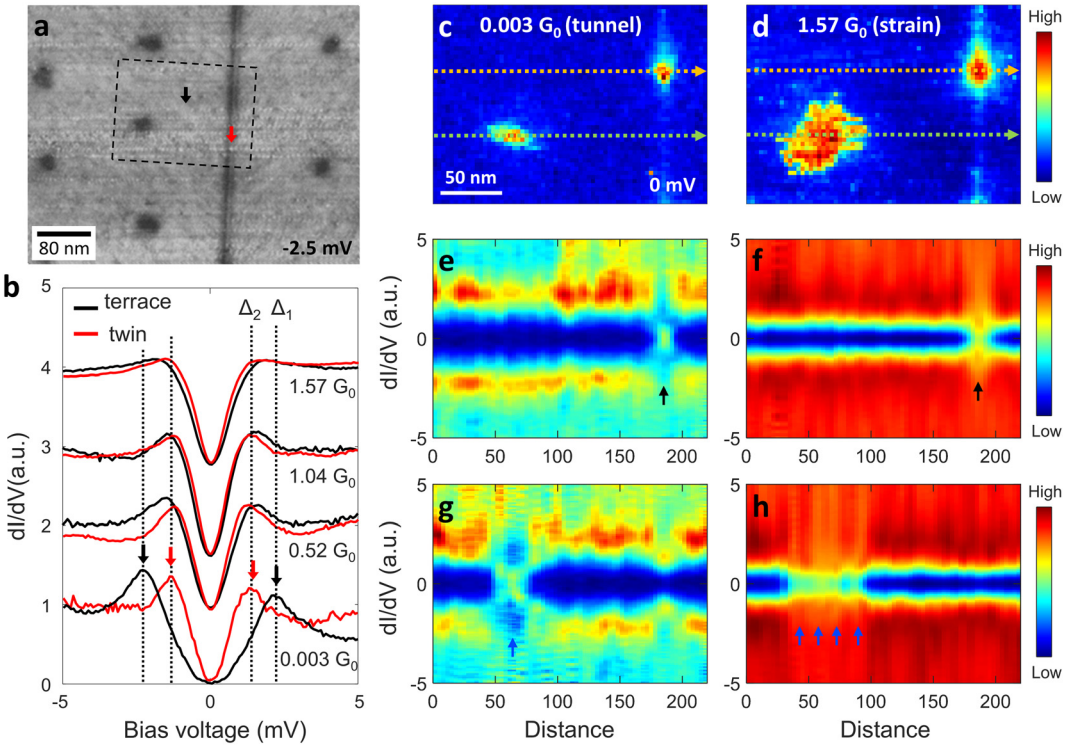


**Fig. 4** Spatial variations of vortex bound states across expanded vortex cores. (a) Conductance map of vortex configuration near a twin boundary. (b) Superconducting gaps at $0.003G_0$ (1 nA), $0.52G_0$ (200 nA), $1.04G_0$ (400 nA), and $1.57G_0$ (600 nA) on the terrace (black spectra) and twin boundary (red spectra). On the terrace, the superconducting gap is changed as the conductance increases, while the superconducting gap remains unchanged on the twin boundary. (c and d) Zero bias conductance maps that contain a vortex on the terrace and a vortex on twin boundary at $0.003G_0$ (1 nA), and $1.57G_0$ (600 nA). Here, $G_0$ is a conductance quantum $2e^2/h$. (e and f) The spatial variations of superconducting gaps across the vortex on the twin boundary (orange dotted arrows in (c and d)) at $0.003G_0$ and $1.57G_0$. (g and h) The spatial variations of superconducting gaps across the vortex on the terrace (green dotted arrows in (c and d)) at $0.003G_0$ and $1.57G_0$. Blue arrows in (h) indicate expanded vortex core.

As seen in the red spectra in Fig. 4b, obtained at the center of the twin boundary (red arrow in Fig. 4a), the energy position of the coherence peaks on the twin boundary are about ±1.2 mV (red arrows in Fig. 4b) in the tunneling regime ($0.003G_0$ (set-point $V_{bias}$ = 5 mV, 1 nA)). The positions of the coherence peaks barely change even at high conductance conditions (red spectra in Fig. 4b) unlike the coherence peaks measured on the terrace (black spectra in Fig. 4b). Moreover, based on our earlier analysis of vortex energetics in FeSe,[42] we conservatively estimate the forces applied to the vortices to be on the order of 1–5 pN (Note S2, SI). This value is several orders of magnitude larger than the previous estimates of mechanical forces applied to isolated vortices in a conventional superconductor.[21] And we conclude that the large susceptibility of the superconducting gap in FeSe to applied strain actually enables applying the forces large enough to displace vortices within dense vortex lattices.

We also found that the apparent size of the vortex core is sensitive to small changes of tip apex, in contrast to topographic features. We observed that a large cluster (cluster 3 in Fig. S9d, SI) on the FeSe surface altered the apex of the STM tip during high conductance mapping ($V_{bias}$ = 2.5 mV, $I$ = 800 nA). We measured differential conductance maps simultaneously with topographic images multiple times while the tip was altered by the cluster (Fig. S9a–f, SI). Notably, the modified tip significantly affected the size of vortex cores, even at the same conductance value (Fig. S9a–c, SI). However, the topographic sizes of structural clusters on the FeSe surface (cluster 1 and cluster 2 in Fig. S9d–f, SI) remain constant (Fig. S9g and h, SI), regardless of the changes in the tip apex. This indicates that the tip apex is quite small, with a tip–surface contact area of only a few nanometers, and the expanded vortex core does not originate from the tip artifact. Meanwhile, the forces acting on the vortices are highly sensitive to the specific shape of the tip apex, suggesting that the geometry of tip-induced wrinkles is dependent on the tip shape.

### Model of tip-induced trapping potential for superconducting vortices

The apparent size of the vortex image can be understood in the context of the bending of the vortex line by the trapping potential from the strain induced inclusion, as schematically shown in Fig. 5a. As defined in ref. 43, we designate the extent of bending in the vortex line as deformation. The red, black, and blue graphs in Fig. 5b show the apparent size of the vortex

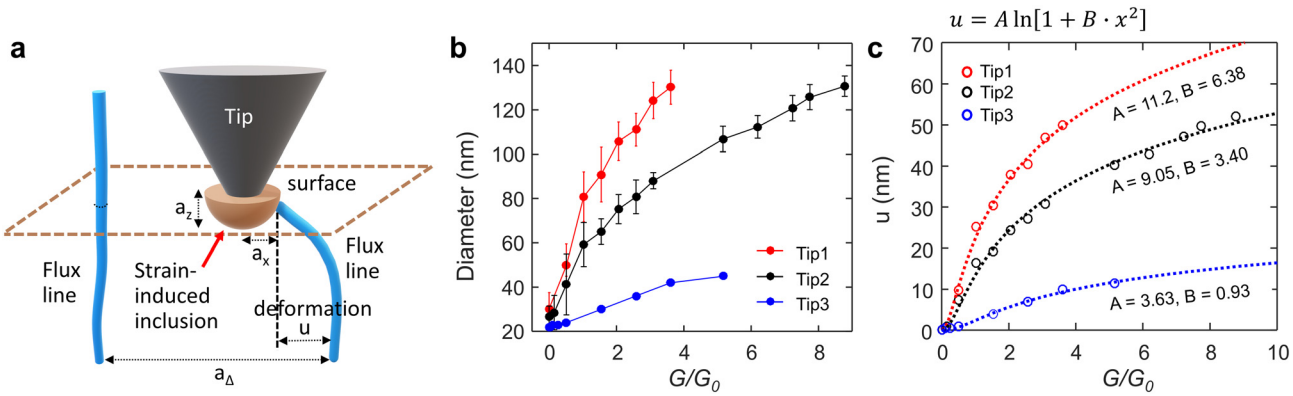


**Fig. 5** Modeling STM junction as a tunable trapping potential. (a) Schematic image of tip induced inclusion and deformed vortex line. (b) Dependences of the diameters of expanded vortex cores on conductance for different tip1 (red), tip2 (black), and tip3 (blue). (c) Dependences of the deformations of vortex lines on the conductance values for tip1 (red circles), tip2 (black circles), and tip3 (blue circles). Each dotted line represents fits based on $A{\cdot}\ln[1 + B{\cdot}x^2]$.

core on the terrace as a function of the conductance for three different STM tip apexes. Each tip apex was reshaped by controlled indentation on a Cu(111) surface. The size of the vortex core logarithmically increases with conductance, but the slope is different for different tip apexes. We plotted graphs for the deformation ($u$) of the vortex line with respect to the conductance obtained from different tip apexes (red, black, and blue circles in Fig. 5c).

We further consider the trapping potential created by the STM tip to be equivalent to an inclusion in the crystal lattice that suppresses superconductivity. In this case, the problem becomes equivalent to vortices interacting with a pinning center in the form of a inclusion with suppressed superconductivity, as previously described by Willa, R. *et al.*[43] The deformation of the vortex line is determined by the elasticity of the vortex line due to the vortex–vortex interaction and the maximum trapping force from the inclusion.[7,43,44] For inclusion sizes comparable to the coherence length ($a_x \sim \xi$), the vortex binding energy to an anisotropic inclusion is given by[44–46]

$$U_p \approx \varepsilon_0 a_z \ln\left(1 + \frac{{a_x}^2}{{\xi_{ab}}^2}\right) \quad (1)$$

where $\varepsilon_0 = {\Phi_0}^2/4\pi\mu_0\lambda^2$ is the typical vortex energy scale, $\lambda$ is the London penetration depth, $a_x$ is the inclusion size along the $x$-axis, $a_z$ is the inclusion size along the $z$-axis, and $\xi_{ab}$ is the coherence length for the $ab$-plane. As detailed in the SI, note S3, we can evaluate the deformation of the vortex line using this formalism. The functional form of the tip-induced force as $A{\cdot}\ln(1 + B{\cdot}x^2)$ provides a very good fit to the experimental data (red, black, and blue dotted lines in Fig. 5c and Fig. S10, SI). Moreover, in this model, we can account for the variability of the deformation by different tip apexes, *via* the effective aspect ratio ($a_z/a_x$) of the tip-induced inclusion. When $a_x$ increases relative to $a_z$ and $a_x > a_z$, the strength of deformation decreases because of the reduced critical angle and distance at which the vortex line enters and exits the inclusion.[43] This means that the shape of the tip apex strongly affects the trapping force and the deformation of the vortex line.

## Conclusions

Our findings show that we can deform individual vortex lines in the surface region of FeSe with nanoscale precision using the STM tip. We revealed how the tip-induced inclusion affects vortex line segments near the surface in FeSe. We confirmed that both twin boundaries and wrinkles in FeSe exhibit suppression of the superconducting gap and act as vortex pinning sites. However, unlike wrinkles that exist only at the surface, the gap-suppressed region at twin boundaries extends into the bulk, thereby forming a stronger pinning potential and even reducing the intervortex distance. By applying strain to the FeSe surface with the STM tip, we created a nanoscale wrinkle beneath the tip, inducing reduction of the superconducting gap and generating an effective trapping potential (inclusion) at arbitrary locations on the surface. Based on a framework provided by established models for pinning, anisotropy, and elasticity caused by defects, we concluded that the STM tip effectively creates a tunable, intermediate-sized anisotropic defect ($a_x \sim \xi$), evolving from a point defect ($a_x < \xi$) as the conductance increases. We also confirmed that the strength of deformation varies significantly depending on the shape of the tip apex. Our governing hypothesis, supported by the spectroscopy measurement, points to local gap reduction as the driving force for the trapping potential. A method of manipulating vortices using the manipulation of pre-existing wrinkles ($a_x \gg \xi$) on $FeTe_{0.55}Se_{0.45}$ and LiFeAs has been reported[47] and strengthens our results. Our results, therefore, provide additional insight into vortex pinning, vortex–vortex interactions, and vortex motion in dense vortex lattices. Moreover, they provide a foundation for building further understanding of the effects of vortex–vortex interactions on accessible manipulation trajectories and the role that intrinsic vortex dynamics can play in quantum information science.

## Materials and methods

We have conducted the experiment using a SPECS Joule-Thompson STM at 1.2 K in the base pressure of $<10^{-10}$ mbar. To precisely approach the STM tip, a SPECS-Nanonis controller was used. We used PtIr tips from UNISOKU. Freshly cleaved surfaces were obtained by delaminating a small sample of FeSe in low vacuum of $<10^{-7}$ mbar, followed by rapid sample transfer to the cryogenic chamber. The differential conductance maps of vortices are obtained using a lock-in technique with the modulation frequency 785 Hz.

## Author contributions

P. M. and S. S. measured and analyzed the data. C. H. and G. B. H. interpreted and provided theoretical input. J. Y. grew FeSe crystals. P. M. and B. J. L. supervised the project. S. S. and P. M. wrote the original draft. B. J. L., C. H., G. B. H., and W. K. contributed to writing. All authors discussed the results and contributed to the manuscript.

## Conflicts of interest

The authors declare that they have no competing interests.

## Data availability

The data supporting the findings of this study are available from the corresponding author upon reasonable request. The Supplementary Information (SI) contains additional STM images, conductance maps, spectroscopy data, and supporting analysis. See DOI: https://doi.org/10.1039/d5nr04204f.

## Acknowledgements

This work was supported by the U.S. Department of Energy, Office of Science, Basic Energy Sciences, Materials Sciences and Engineering Division. Scanning tunneling microscopy was performed at the Center for Nanophase Materials Sciences (CNMS), which is a US Department of Energy, Office of Science User Facility at Oak Ridge National Laboratory.

## References

1 A. A. Abrikosov, *Sov. Phys. JETP*, 1957, **5**, 1174.
2 P. G. De Gennes and J. Matricon, *Rev. Mod. Phys.*, 1964, **36**, 45.
3 P. H. Borcherds, C. E. Gough, W. F. Vinen and A. C. Warren, *Philos. Mag.*, 1964, **10**, 349.
4 G. Blatter, M. V. Feigel'man, V. B. Geshkenbein, A. I. Larkin and V. M. Vinokur, *Rev. Mod. Phys.*, 1994, **66**, 1125.
5 G. Blatter, V. B. Geshkenbein and J. A. G. Koopmann, *Phys. Rev. Lett.*, 2004, **92**, 067009.
6 O. M. Auslaender, L. Luan, E. W. J. Straver, J. E. Hoffman, N. C. Koshnick, E. Zeldov, D. A. Bonn, R. Liang, W. N. Hardy and K. A. Moler, *Nat. Phys.*, 2009, **5**, 35.
7 W.-K. Kwok, U. Welp, A. Glatz, A. E. Koshelev, K. J. Kihlstrom and G. W. Crabtree, *Rep. Prog. Phys.*, 2016, **79**, 116501.
8 C. W. J. Beenakker, *Annu. Rev. Condens. Matter Phys.*, 2013, **4**, 113.
9 D. Wang, L. Kong, P. Fan, H. Chen, S. Zhu, W. Liu, L. Cao, Y. Sun, S. Du, J. Schneeloch, R. Zhong, G. Gu, L. Fu, H. Ding and H.-J. Gao, *Science*, 2018, **362**, 333.
10 T. Machida, Y. Sun, S. Pyon, S. Takeda, Y. Kohsaka, T. Hanaguri, T. Sasagawa and T. Tamegai, *Nat. Mater.*, 2019, **18**, 811.
11 M. Li, G. Li, L. Cao, X. Zhou, X. Wang, C. Jin, C.-K. Chiu, S. J. Pennycook, Z. Wang and H.-J. Gao, *Nature*, 2022, **606**, 890.
12 A. Yu. Kitaev, *Ann. Phys.*, 2003, **303**, 2.
13 S. Das Sarma, M. Freedman and C. Nayak, *Phys. Rev. Lett.*, 2005, **94**, 166802.
14 J. C. Y. Teo and C. L. Kane, *Phys. Rev. Lett.*, 2010, **104**, 046401.
15 X. Ma, C. J. O. Reichhardt and C. Reichhardt, *Phys. Rev. B*, 2020, **101**, 024514.
16 D. A. Ivanov, *Phys. Rev. Lett.*, 2001, **86**, 268.
17 M. Sato and S. Fujimoto, *Phys. Rev. B:Condens. Matter Mater. Phys.*, 2009, **79**, 094504.
18 X. Ma, C. J. O. Reichhardt and C. Reichhardt, *Phys. Rev. B*, 2018, **97**, 214521.
19 I. S. Veshchunov, W. Magrini, S. V. Mironov, A. G. Godin, J.-B. Trebbia, A. I. Buzdin, P. Tamarat and B. Lounis, *Nat. Commun.*, 2016, **7**, 12801.
20 J.-Y. Ge, V. N. Gladilin, J. Tempere, C. Xue, J. T. Devreese, J. Van de Vondel, Y. Zhou and V. V. Moshchalkov, *Nat. Commun.*, 2016, **7**, 13880.
21 A. Kremen, S. Wissberg, N. Haham, E. Persky, Y. Frenkel and B. Kalisky, *Nano Lett.*, 2016, **16**, 1626.
22 J. T. Zhang, J. Kim, M. Huefner, C. Ye, S. Kim, P. C. Canfield, R. Prozorov, O. M. Auslaender and J. E. Hoffman, *Phys. Rev. B:Condens. Matter Mater. Phys.*, 2015, **92**, 134509.
23 N. Shapira, Y. Lamhot, O. Shpielberg, Y. Kafri, B. J. Ramshaw, D. A. Bonn, R. Liang, W. N. Hardy and O. M. Auslaender, *Phys. Rev. B:Condens. Matter Mater. Phys.*, 2015, **92**, 100501.
24 A. Yagil, Y. Lamhot, A. Almoalem, S. Kasahara, T. Watashige, T. Shibauchi, Y. Matsuda and O. M. Auslaender, *Phys. Rev. B*, 2016, **94**, 064510.
25 E. W. J. Straver, J. E. Hoffman, O. M. Auslaender, D. Rugar and K. A. Moler, *Appl. Phys. Lett.*, 2008, **93**, 172514.
26 I. Keren, A. Gutfreund, A. Noah, N. Fridman, A. Di Bernardo, H. Steinberg and Y. Anahory, *Nano Lett.*, 2023, **23**, 4669.
27 T. Golod, L. Morlet-Decarnin and V. M. Krasnov, *Nat. Commun.*, 2023, **14**, 4926.
28 S. A. Díaz, J. Nothhelfer, K. Hals and K. Everschor-Sitte, *Phys. Rev. B*, 2024, **109**, L201110.

29 C.-K. Chiu, T. Machida, Y. Huang, T. Hanaguri and F.-C. Zhang, *Sci. Adv.*, 2020, **6**, eaay0443.
30 W. Liu, L. Cao, S. Zhu, L. Kong, G. Wang, M. Papaj, P. Zhang, Y.-B. Liu, H. Chen, G. Li, F. Yang, T. Kondo, S. Du, G.-H. Cao, S. Shin, L. Fu, Z. Yin, H.-J. Gao and H. Ding, *Nat. Commun.*, 2020, **11**, 5688.
31 T. Zhang, W. Bao, C. Chen, D. Li, Z. Lu, Y. Hu, W. Yang, D. Zhao, Y. Yan, X. Dong, Q.-H. Wang, T. Zhang and D. Feng, *Phys. Rev. Lett.*, 2021, **126**, 127001.
32 J. A. Stroscio and D. M. Eigler, *Science*, 1991, **254**, 1319.
33 M. F. Crommie, C. P. Lutz and D. M. Eigler, *Science*, 1993, **262**, 218.
34 P. Maksymovych, in *Scanning Probe Microscopy of Functional Materials: Nanoscale Imaging and Spectroscopy*, ed. S. V. Kalinin and A. Gruverman, Springer, New York, 2011, pp. 3–37.
35 G. Pristáš, S. Gabáni, E. Gažo, V. Komanický, M. Orendáč and H. You, *Thin Solid Films*, 2014, **556**, 470.
36 P. O. Sprau, A. Kostin, A. Kreisel, A. E. Böhmer, V. Taufour, P. C. Canfield, S. Mukherjee, P. J. Hirschfeld, B. M. Andersen and J. S. Davis, *science*, 2017, **357**, 75.
37 S. Y. Song, G. B. Halász, J. Yan, B. J. Lawrie and P. Maksymovych, arXiv, 2025, preprint, arXiv:2506.16384, DOI: 10.48550/arXiv:2506.16384.
38 A. E. Böhmer, F. Hardy, F. Eilers, D. Ernst, P. Adelmann, P. Schweiss, T. Wolf and C. Meingast, *Phys. Rev. B:Condens. Matter Mater. Phys.*, 2013, **87**, 180505.
39 A. E. Böhmer, T. Arai, F. Hardy, T. Hattori, T. Iye, T. Wolf, H. v. Löhneysen, K. Ishida and C. Meingast, *Phys. Rev. Lett.*, 2015, **114**, 027001.
40 C.-L. Song, Y.-L. Wang, Y.-P. Jiang, L. Wang, K. He, X. Chen, J. E. Hoffman, X.-C. Ma and Q.-K. Xue, *Phys. Rev. Lett.*, 2012, **109**, 137004.
41 T. Watashige, Y. Tsutsumi, T. Hanaguri, Y. Kohsaka, S. Kasahara, A. Furusaki, M. Sigrist, C. Meingast, T. Wolf, H. v. Löhneysen, T. Shibauchi and Y. Matsuda, *Phys. Rev. X*, 2015, **5**, 031022.
42 S. Y. Song, C. Hua, L. Bell, W. Ko, H. Fangohr, J. Yan, G. B. Halász, E. F. Dumitrescu, B. J. Lawrie and P. Maksymovych, *Nano Lett.*, 2023, **23**, 2822.
43 R. Willa, A. E. Koshelev, I. A. Sadovskyy and A. Glatz, *Phys. Rev. B*, 2018, **98**, 054517.
44 A. E. Koshelev and A. B. Kolton, *Phys. Rev. B:Condens. Matter Mater. Phys.*, 2011, **84**, 104528.
45 C. J. Van Der Beek, M. Konczykowski, A. Abal'oshev, I. Abal'osheva, P. Gierlowski, S. J. Lewandowski, M. V. Indenbom and S. Barbanera, *Phys. Rev. B:Condens. Matter Mater. Phys.*, 2002, **66**, 024523.
46 C. J. van der Beek, M. Konczykowski and R. Prozorov, *Supercond. Sci. Technol.*, 2012, **25**, 084010.
47 P. Fan, H. Chen, X. Zhou, L. Cao, G. Li, M. Li, G. Qian, Y. Xing, C. Shen, X. Wang, C. Jin, G. Gu, H. Ding and H.-J. Gao, *Nano Lett.*, 2023, **23**, 4541.